IISc THESES ABSTRACTS

Thesis Abstract (M. Sc. (Engng))

Development of a particle image velocimeter and its applications in low speed jets by
G. Ramesh
Research supervisors: Prof. R. M. Vasu and Dr K. T. Madhavan (NAL)
Department: Instrumentation

1. Introduction

Particle image velocimetry (PIV) is a whole-field measurement technique where the flow velocities in a plane of interest are obtained with high temporal and spatial resolution. The need for such a simultaneous multi-point measurement is acute in unsteady turbulent flow where it is widely recognised that the instantaneous realisation of the flow may bear little resemblance to the average structure. Early work on PIV to flow measurement was reported by Meynnart[1] and Adrain.[2] The measuring principle of PIV is that instantaneous fluid velocities can be evaluated by recording the positions of images produced by small traces present in the fluid at successive time instants. The basic assumption is that these trace particles follow the flow closely.

In the present work, development of PIV using a continuous wave laser for the measurement of two-dimensional velocity vectors at low-speed flows is reported. This includes the development of a recording system to image the seed particles in the flow at precisely known interval and PC-based offline data-processing systems to extract 2D velocity vectors from the PIV records.

2. Methodology

A 5W Ar–Ion laser is used as a light source and the collimated beam is externally chopped using a mechanical shutter to give a pulse repetition rate in the range of 1–50 ms. A light sheet optics using a set of convex and cylindrical lenses was used to form a thin light sheet (~1 mm thick) with a *top hat* intensity profile in an area of about 200×200 mm. The flow fields under study were the near fields of circular and elliptic jets in ambient water. The schematic of the circular nozzle assembly is also shown in the above figure. The horizontal jet flow from the nozzle was maintained in a glass tank of $600 \times 300 \times 200$ mm and the level of the tank was maintained constant. A Nikon SLR camera (FM 2) with a Nicor 0.55 mm objective lens was used for capturing double-exposed images. High-speed photographic film (Kodak 3200 ASA) was used due to its high spectral sensitivity. Best results were obtained with glass hollow spheres (mean diameter ~ 8 μm) as seed particles.

PIV records in the form of double/multiple exposed photographic negatives were processed offline using (i) Young's fringe analysis (in the case of images with high particle density), and (ii) 2D autocorrelation (for sparsely seeded flow). A low-power He–Ne laser (15 mW) beam scans the double-exposed negative in steps of 0.5 mm. A computer-controlled 2D transverse
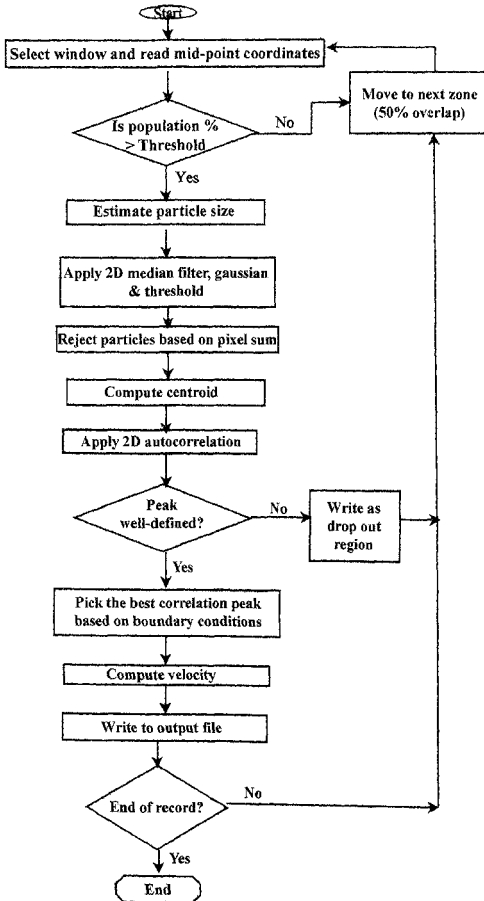
FIG. 1. Flowchart for vector extraction using autocorrelation.

developed for this purpose holds the film and positions it precisely to the laser beam. At each position, the Young's fringes obtained in the Fourier plane of the film is imaged using a mono-chrome CCD camera and digitized as 8-bit gray scale image with the frame size of 256×256. The program developed in MATLAB for the Young's fringe analysis uses 1D averaging[3] and 2D FFT methods. The fringe spacing and orientation were determined with higher speed and accuracy with the 2D FFT scheme.

In the case of PIV recordings with low seeding density an autocorrelation approach is used for the extraction of particle displacement and angle. Unlike a standard PIV system this scheme does not use any sophisticated image-recording system like CCD camera or array processor with high-end imaging libraries. This novel method uses a general-purpose desk scanner to digitize (with the aspect ratio retained) the enlarged PIV images at 100-dpi resolution with 8-bit gray-scale depth. An efficient preprocessing algorithm was developed to process noisy records. This scheme uses a heuristic kernel[4] (similar to a gaussian) to identify valid particles and the efficiency of this scheme is demonstrated from the low percentage of spurious vectors (less than 10%) in a high-gradient flow (impulsively started jet). The flowchart for the vector extraction using autocorrelation is given in Fig. 1.

3. Results and conclusion

It is observed that quadruple pulsing scheme for PIV records produced higher detectability ratio for autocorrelation analysis. In the case of high-density particle images the 2D FFT scheme is found to be faster and more accurate compared to the well-known 1D averaging scheme proposed by Robinson.[3] The PIV system is validated from the measurement in an axisymmetric jet (in ambient water) at low velocities and the results (Fig. 2) were compared with standard LDV measurements. The scatter in the centre line velocities is less than 5% in the potential core (up to 5 diameters) at low turbulent Reynolds number (~ 3000). The comparison of streamwise velocity components along the axial and radial directions up to five diameters was found to be encouraging despite the fact that only a few records were used for estimation of flow statistics. The time-consuming and tedious photographic development basically limited the sample sizes. The study of PIV technique in an elliptical jet of small aspect ratio (2:1) clearly demonstrated the axis-switching at about four (major) diameters (Fig. 3). Such a phenomenon is perhaps observed using PIV technique for the first time.
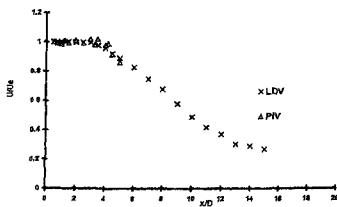

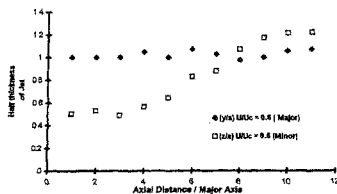FIG. 2. Centre line velocity comparison of PIV and LDV in the near field of axisymmetric jet. (*ReD* ~3000).

FIG. 3. Features of the axis switch in elliptic jet. ($a/b = 2$, Re ~ 4100)

References

1. MEYNART, R.   Instantaneous velocity field measurements in unsteady gas flow by
                                  speckle velocimetry, *Appl. Opt.*, 1983, **22**, 535–540.

2. ADRIAN, R.   Scattering particle characteristics and their effect on pulsed laser
                                  measurements of fluid flow: Speckle velocimetry vs particle image
                                  velocimetry, *Appl. Opt.*, 1984, **23**, 1690–1691

3. ROBINSON, D. W   Automatic fringe analysis with a computer image processing sys-
                                  tem, *Appl. Opt.*, 1983, **22**, 2474–2476.

4 BALLARD, H. D AND BROWN, M C.   *Computer vision*, Ch. 3, Prentice Hall, 1982

Thesis Abstract (M. Sc. (Engng))

Studies on plate impact by S. Ramachandra
Research supervisors: Prof. K. R. Y. Simha and Dr K. Ramachandra (GTRE)
Department: Mechanical Engineering

1. Introduction

Aerospace, marine and automobile components are frequently subjected to impact loading. To complicate matters, these components are thin plates and shells to reduce overall structural weight. The problem of a sphere impacting a large flat plate forms the subject of this work. The plate impact problem has been of major concern from the early part of this century.[1, 2] This work is an attempt to capture the essential aspects of dynamic strains in plates when one or two projectiles are impacted. Double-projectile impact is a new contribution to this field and represents reality better. A major part of this work is experimental with an objective to record and interpret impact strains. A wide range of projectile velocities (2–240 m/s) is covered by performing drop and launch tests using an air gun. Dynamic strains were measured in two orthogonal directions at various strain gauge stations around the impact site.

Major unknowns in impact mechanics, viz. impact force, impulse and energy quantities are extremely sensitive to mechanical properties and impact parameters. To estimate the above quantities for a given set of materials of the target and the impactor calls for a strategic deployment of instrumentation around the impact site. Any instrument deployed should not be too close lest it gets damaged and at the same time not too far too as signals get increasingly obscured by spurious reflections from the boundaries. It is also necessary to ensure high-speed recording with reliable high-frequency response.

2. Experimental procedures and results

For the present work, the problem of impact of steel spheres on titanium plate has been chosen as titanium has wide aerospace application. Spherical projectiles were chosen as the contact between the target and sphere would remain similar in the event of slight obliquity unlike in cases of cylindrical or cylindro-conical projectiles. Thickness of plate is constant for all experiments.

For the current study, two types of tests are planned. The first set of experiments is conducted using drop tests, their advantage being better control on velocity and location of impact and ease of operation. Another set of experiments is planned using a 150 mm airgun facility at the Gas Turbine Research Establishment. The basic aim of the experiment is to record strains due to impact at various radial locations. In addition, other parameters like contact duration and velocity of impact are also recorded. Velocity is computed using the height of drop neglecting air resistance.

3. Theory and discussion of results

When an infinite homogenous, isotropic linear elastic plate is subjected to a normal concentrated impact load, producing an impulse J, a fundamental solution for plate motion $w(r, t)$ given by Medick[3] and Sneddon[4] is:

$$w(r,t) = \frac{J}{4\pi(\rho hD)^{1/2}}\left[\frac{\pi}{2} - Si\left(\frac{ar^2}{t}\right)\right]$$

$$a = \frac{1}{4}\left(\frac{\rho h}{D}\right)^{1/2} = \frac{\sqrt{3}}{2hC_0}; C = \sqrt{\frac{E}{\rho}}; D = \frac{Eh^3}{12(1-v^2)}$$

where $w(r, t)$ is transverse displacement, D the plate bending stiffness, ρ the mass density, h the plate thickness, v the Poisson's ratio, r the radial distance form the impact site and t time.

Tangential and radial strains are:

$$\varepsilon_\theta = \left[\frac{Kh}{r^2}\right]\sin\left(\frac{ar^2}{t}\right)$$

$$\varepsilon_r = \left[\frac{Kh}{r^2}\right]\left[2x\cos\left(\frac{ar^2}{t}\right) - \sin\left(\frac{ar^2}{t}\right)\right]$$

The tangential strain decays more gradually with time as compared to radial strain. The signal patterns for double impact are similar to those under single impact.

4. Conclusions

The fundamental problem of a spherical projectile impacting a large thin plate provides a convenient starting point for engineering design. Initial transients carry vital information of the impact phenomena.[5] This work makes an attempt to highlight experimental strategies to record impact-generated dynamic strains when one and two projectiles are involved. The latter situation involving two projectiles can be a starting point for multiple impact studies. A vast amount of experimental data, gathered in the course of this investigation, proved useful in verifying an impulse-response model of plate motion which was developed as a part of this work. This model was further used to develop a relation for force–time history deconvolution and to study the double-projectile impact situation.

References

1. RAMAN, C. V.   On some applications of Hertz's theory of impact, *Phys. Rev.*, 1920, **15**, 277–284.

2. GOLDSMITH, W.   *Impact*, Edward Arnold, 1960.

3. MEDICK, M. A.   On classical plate theory and wave propagation, *J. Appl. Mech.*, 1961, 223–228.

4. SNEDDON, I. N   *Fourier transforms*, McGraw-Hill, 1951, p. 134

5. RAMACHANDRA, S., SIMHA, K. R. Y. AND RAMACHANDRA, K   Signatures of transients in plate impact, *Proc. NASAS Conf.*, Bangalore, August 1997, pp. III 259–264.

Thesis Abstract (M. Sc. (Engng))

Compressive creep characterization of polycrystalline 8 mol% yttria-stabilized cubic zirconia by B. Sudhir
Research supervisor: Atul H. Chokshi
Department: Metallurgy

1. Introduction

Yttria-stabilized cubic zirconia is a good oxygen ion conductor that is used in many high-temperature functional applications such as oxygen sensors, combustion controls for furnaces and solid oxide fuel cells.[1] At higher temperature, the properties of a material become significantly time dependent; this can be characterized by studying the creep behaviour of the material.

Creep refers to the time-dependent deformation of a material under an applied load. It is a thermally activated process and becomes significant at higher temperatures (> 0.4 T_m, where T_m is the melting point of the material). Creep study typically involves the study of the dependence of creep rate on grain size, temperature and stress, and a relation showing such dependence can be written as:

$$\dot{\varepsilon} = A \frac{DGb}{KT} \left(\frac{\sigma}{G}\right)^n \left(\frac{b}{d}\right)^p \tag{1}$$

where $\dot{\varepsilon}$ is the steady-state creep rate, A the dimensionless constant, D the diffusion coefficient, G the shear modulus, b the magnitude of the Burger's vector, k Boltzmann's constant, T the absolute temperature, σ the imposed stress, n is termed the stress exponent, d the grain size and p the inverse grain size exponent. The diffusion coefficient may be expressed as $D = D_0 \exp(-Q/RT)$, where D_0 is a frequency factor, Q the activation energy and R the gas constant. The values, n, p and Q, are specific to a creep mechanism and are termed creep parameters.

In polycrystalline materials grain growth becomes significant as temperature increases[1,2] and there is also a possibility of deformation enhancing grain growth (called dynamic grain growth).[3] As grain growth affects creep (eqn (1)), it is necessary to study grain size evolution to characterize creep behaviour.

Grain growth refers to the time-dependent increase in the mean size of grains in a polycrystalline material. The driving force is the minimization of the extra energy associated with the grain boundaries, but the kinetics is governed by the grain boundary mobility.[2] An equation for static grain growth may be written as:

$$d^N - d_0^N = K_g t \tag{2}$$

where d is the grain size at time t, d_0 the initial grain size, N the grain growth exponent, K_g the grain growth constant and may be expressed as

$$K_g = K' \exp(-Q_g/RT)$$

where K' is a constant and Q_g the activation energy for grain growth.

The aim of the present study was to characterize the creep behaviour of polycrystalline 8 mol% yttria-stabilized cubic zirconia (8YCZ) in terms of (a) dependence of creep on stress, grain size and temperature, and (b) comparison of static and dynamic grain growth.

2. Experimental

The 8YCZ used in the present study was obtained in the form of presintered sheets (>99% of the theoretical density) from which samples for grain growth and creep were cut.

2.1. *Grain growth study*

Static grain growth studies were done in a temperature range of 1673–1873 K and for durations of 2 to 30 h. The samples were polished, chemically etched using boiling ortho-phosphoric acid and their optical micrographs taken, from which the grain sizes were measured using mean linear intercept method. For dynamic grain growth studies, the crept samples were cut along loading axis and grain sizes determined by measuring grain intercepts in two directions: along and perpendicular to loading axis; this facilitated the measurement of the grain aspect ratio.

2.2. *Creep study*

Parallelepiped samples of ~$3 \times 3 \times 5$ mm dimensions were used and creep tests were conducted in the temperature range of 1673–1773 K, stresses of 20 to 200 Mpa and grain sizes of ~4.5 to 8 μm. The experiments were carried out in a lever-type machine fitted with a load cell, a displacement transducer and a stepper motor. These were interfaced to a computer and had the provision to keep the stress constant by using a closed loop control.

2. Results and discussion

3.1. *Grain growth study*

Under static growth conditions used, the grain sizes varied from about 4 to 13 μm. The grain growth exponent N was found to be 2 and the activation energy for grain growth was 270 ± 80 kJ mol^{-1}. The grain growth data are in agreement with those reported by Lee *et al.*[4] and Zhou *et al.*[5] on the same material. An N value of 2 (called parabolic growth rate) is ex-

pected when grain growth is controlled by grain boundary curvature, and a value of 3 is expected if the boundary experiences a drag force because of solute segregation to the grain boundary.[2]

The grain growth activation energy for parabolic growth rate is expected to be the grain boundary activation energy for the diffusion of the rate-controlling ion[2] (zirconium ion in the present case[6]). In the crept samples, the grains did not show any observable change in the grain aspect ratio and the grain sizes were comparable to those obtained under static grain growth conditions, indicating that the stresses used in the present study did not affect grain growth. However, the grain growth in the crept samples was significant (> 10%) and so it had to be considered while determining creep parameters.

3.2. *Creep study*

For the experimental conditions used, the strain rates varied from 10^{-8} to 10^{-3} s^{-1} and the creep curves exhibited all the three stages: primary, secondary (also called steady state) and tertiary. The duration of the secondary stage was found to decrease with an increase in either stress, temperature or grain size; the maximum strain achieved in the secondary region was ~5% and at stresses above ~80 Mpa there was no discernible secondary region.

Initially, experiments were conducted well into the tertiary to ensure the presence of a genuine steady state. As there was significant grain growth, subsequent creep experiments were stopped in the steady state, the final grain sizes (d) were measured and used to determine the creep parameters. There was a transition in the apparent stress exponent (stress exponent calculated by using the initial grain size) from a value of ~2 at lower stresses to ~11 at higher stresses (> 80 MPa). The high stress region is expected to occur due to some form of material degradation mechanism that could not be identified. In the low stress region, the inverse grain size exponent was 3.3 ± 0.6 and the actual stress exponent, obtained by compensating the strain rate for grain growth, i.e., $\dot{\varepsilon} d^{33}$, was 1.3 ± 0.6. The activation energy could be calculated from only two temperatures and was not reliable; it was about 360 kJ mol^{-1}. The creep parameters are comparable to the values of $n = 1$ and $p = 3$ predicted by the Coble creep model[7] with the creep rate being controlled by the grain boundary diffusion of zirconium ion.[6] However, the errors in the parameters are such that the other grain boundary-based creep models, such as Nabarro–Herring and interface reaction,[8] cannot be ruled out.

4. Summary and conclusion

In the present study, the grain growth and compressive creep behaviour of 8YCZ were characterized in the temperature range of 1673–1773 K, stresses of 20 to 200 MPa and grain sizes of ~4.5 to 8 μm. Grain growth followed the parabolic growth law and deformation conditions used in the present study did not have any observable effect of the grain growth behaviour. There was significant grain growth during creep testing but it was attributable to static grain growth. The material could not be tested to higher strains or at stresses because it entered the tertiary at strains less than 5% and did not exhibit any secondary region at stresses higher than 80 Mpa. In the low stress region, the material exhibited a stress exponent of 1.3 ± 0.6 and an inverse grain size exponent of 3.3 ± 0.8, which agree with those predicted by Coble creep mechanism

References

1	SUBBARAO, E. C.	*Advances in ceramics*, Vol. 3, American Chemical Society, 1981, pp. 1–24
2.	BENNISON, S. J	*Engineering material handbook*, Vol. 4, ASM International, 1991, pp. 304–312.
3.	NEILI, T. G AND WADSWORTH, J.	*J. Am. Ceram. Soc.*, 1989, **72**, 1469–1472.
4.	LEE, I. G. AND CHEN, I. W.	*Sintering '87*, Vol. 1, Elsevier, 1988, pp. 304–345.
5.	ZHOU, Y. *et al*	*Ceram. Int*, 1992, **18**, 237–242.
6.	OISHI, Y *et al.*	*Advances in ceramics*, Vol. 7, American Chemical Society, 1983, pp. 208–219.
7	COBLE, R. L.	*J. Appl. Phys*, 1963, **34**, 1679–1682.
8	HYNES, A. AND DOREMUS, R.	*Cr. Rev. Solid St. Mater. Sci.*, 1996, **21**, 129–187

Thesis Abstract (M. Sc. (Engng))

Utilisation of a 3-phase self excited induction generator for microhydel power plants by
Sundeep Kohli
Research supervisor: Prof. V. Ramanarayanan
Department: Electrical Engineering

1. Introduction

Electric power is vital part of modern living. Conventionally, the demand for power is met by coal-, oil-fired or hydroelectric power plants. Power generated in these plants is transmitted to load centres (i.e. places where demand of electricity is high). In remote locations, where transmission of power from remote generators is prohibitively expensive, the trend is to tap energy from local sources. In places, where water streams are in abundance, demand of power can be met by stand-alone micro hydel power plants (MHPP). Induction machines are standard, inexpensive and repair skills of such machines are available in remote areas. The self-excited induction generators (SEIG) are preferred in MHPPs. The self-excitation of induction generator with capacitors connected to the output is well known.[1–2] The feasibility of utilising SEIG for MHPP has been explored. It is assumed that MHPPs cater to purely resistive load. On account of small capacities, the loads are predominantly single phase. A three-phase induction generator can be used for a single-phase resistive load by using load-balancing elements.[3–4] MHPP are meant for low capacities; therefore it is not economical to apply mechanical governing for these plants. The water head is constant so the streams have constant flow of water. Hence, the power input to the turbine is nearly constant. Voltage and frequency can be regulated by keeping the output power constant. This is called load governing. A ballast load is connected parallel to the main load. When the main load varies, ballast load is changed in such a way as to keep the effective load (sum of main and ballast loads) constant. The frequency and voltage vary due to variations in load. It is possible to sense variations in load by sensing the line voltage and the power to the ballast load is changed such that the line voltage remains constant.

This is called the voltage feedback control which is implemented. The dynamic model of the system (i.e. SEIG and load governor using voltage feedback control) is described. The simulation is done in SIMULINK (a toolbox of MATLAB software package) and the results are presented. Finally, simulation results are compared with test results.

2. Dynamic model of an SEIG

The induction machine can be utilised as a generator if supply of reactive power is available for providing excitation to the machine. For the stand-alone operation of an induction generator, self-excitation is achieved by connecting capacitors across the machine terminals.[1, 2] The process of self-excitation is initiated by the residual magnetism present in the machine or by electric charge present on the capacitors. Figure 1 shows the approximate per phase equivalent circuit of the SEIG at no load, when the slip is zero and core losses are neglected. The magnetising current (I_m) and the magnetising EMF (E_m) are shown in Fig. 2. Typical nonlinear magnetisation characteristics of an induction machine are represented by Curve 5 in Fig. 2. Curve 1 represents the capacitive reactance of capacitance C_e. Curves 1 and 5 intersect at points O and c. Points O and c are two equilibrium points. Point O is unstable equilibrium point and a very small perturbation due to a small charge at capacitor terminals or a small residual magnetism of the machine initiates the process of self-excitation. Finally, the stable equilibrium point c is reached. The same process will take place in case of Curves 3 and 2 (where the stable equilibrium points are a and b, respectively, corresponding to different values of excitation capacitance). Curve 4 corresponds to a very low value of excitation ca-pacitance. Curve 4 and 5 intersect at point O (Fig. 2). In this case, O is the only equilibrium point. The capacitance corresponding to Curve 4 is insufficient to achieve voltage build up in the machine. The capacitance corresponding to Curves 2 and 3, though can initiate build up, do not provide adequate output voltage. Capacitance C_e corresponding to Curve 1 is seen to be proper for build up and operation around rated output voltage. For build up to occur and self-excitation to be established, there is a minimum value of capacitance to be connected across the terminals, which is determined from the magnetisation characteristics of the induction machine.

Magnetisation characteristics are determined experimentally. The induction machine is given 3-phase ac supply through an auto transformer and simultaneously is driven by a dc machine too. A line-frequency stroboscope is used to check the speed of the machine. The dc machine is used as a prime mover to run the induction machine at synchronous speed corresponding to the line frequency supplied to the induction machine. The idea is to keep the slip at zero. Now the ac input voltage to the induction machine is varied up to 120% of the rated value. The line voltage, line current and no load power are obtained from the experiment. The per-phase
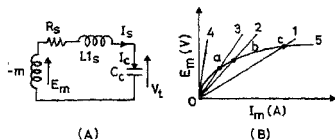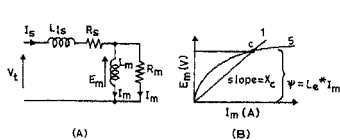

FIG. 1.

FIG. 2.

circuit of an induction machine at zero slip is shown in Fig. 3. The machine parameters (stator leakage inductance (L_{ls}), rotor leakage inductance (L_{lr}), rotor-winding resistance (R_r) and stator winding resistance (R_s)) are determined through standard tests (no load and blocked rotor tests). The core loss resistance (R_m) is also determined. The core loss component of current (I_{mr}) is also shown in Fig. 3. The per-phase voltage (V_t), stator current (I_s) and no load power (W_{nl}) are calculated (depends if the machine is connected in star or delta). The magnetising current (I_m) and magnetising emf (E_m) are calculated from Fig. 3. From E_m, I_m and f (line frequency), the effective inductance (L_e) of magnetizing branch and effective flux linkages (ψ) are calculated.

Inductive reactance (X_e) is the slope of line oc in Fig. 3.

$$X_c = E_m/I_m \text{ and } L_e = X_m/2*\pi*\phi.$$

Flux linkages at corresponding to point C are given as,

$$\psi = Im*Le.$$

Curve-fitting tools are used to express effective inductance (L_e) as a function of effective flux linkages (ψ) and are given by

$$L_e = f(\psi) \tag{1}$$

A dynamic model of SEIG is developed from the basic model of an induction machine. Standard dynamic models of induction machine in α–β coordinates[5] are used to develop the dynamic model of SEIG. The magnetising inductance is modelled by eqn 1. The speed of machine is assumed to be constant. The above model is used for simulation. The voltage build up with different excitation capacitance, load and speeds is obtained from simulation. The results obtained from the simulated model match the experimental performance to within 10% and are considered satisfactory.

3. Loading of an SEIG

The typical frequency and voltage regulation for the generator used for experiments is 7 and 30%, respectively. Therefore, while delivering 50 Hz at rated power, prime mover speed is kept at 1.07 p.u. (i.e. 1600 rpm for a 4-pole machine). Under this condition we wish to obtain maximum output power from the given SEIG (without exceeding voltage and current ratings of the machine). This is done by connecting appropriate excitation capacitance (as explained in Section 2) and load resistance across the machine terminals. The per-phase equivalent circuit of the output of the SEIG is shown in Fig. 3. The figure also shows parallel combination of load resistance (R) and excitation capacitance (C_e). Maximum output power is obtained when the capacitive reactance is equal to load resistance. This condition is given by eqn 2 (X_{ce} is capacitive reactance due to excitation capacitance).

$$I_{load} = I_C. \tag{2}$$

If the machine current is equal to its rated value, then the maximum power is transferred when the magnitude of the capacitive current is equal to the load current (same as the condition of eqn 2). Therefore, it is possible to load the SEIG up to 0.71 times of its kVA rating (if line voltage of 1 p.u. is built at point c). There can be further derating on account of drop in voltage as generator is loaded (which depends on the machine). The load is predominantly single

phase. The single-phase resistive load can be balanced by using load-balancing schemes.[3, 4] The resistive load is connected across phases Y and B. The currents can be balanced by connecting inductance (X_L is inductive reactance) across phases Y and R and connecting capacitance (X_C is capacitive reactance) across phases R and B. The conditions given in eqns 3 and 4 should be met.

$$R = 1.732* |X_C| \tag{3}$$

$$R = 1.732* |X_L| \tag{4}$$

The rating of the generator used for testing was 2.2 kW (and 3.4 kVA). This generator was loaded up to 2.1 kW by using the loading-balancing scheme (mentioned above).

4. Voltage regulation of an SEIG

In Fig. 4a, an SEIG is shown with ballast load. A single-phase resistive load is connected across terminals Y and R. The load-balancing elements, inductor (L_C) and capacitor (C_C) are connected between Y and B, and B and R, respectively. A ballast load (R_a) is connected parallel to the main load (R_L), across Y and R. The frequency and magnitude of the line voltage vary with variations in load. In the full range of load variation the frequency changes by 7%, whereas line voltage changes by 25–30%. The voltage and frequency regulation is achieved if the sum of the main and ballast loads is maintained constant (i.e. effective load across the terminals Y and R is maintained constant). It is possible to sense variations in load by sensing line voltage and power to the ballast load is changed such that the line voltage remains constant. In this way, effective load is maintained constant.

The ballast load resistance is connected on the DC side with a series switch S (Fig. 4). The switching frequency is 25 kHz. The power to the ballast load is controlled through the duty ratio of the switch. When the switch is always on, the duty ratio is unity and the ballast load resistance is minimum (i.e. equal to R_a or load is maximum). When the switch is always off, the duty ratio is zero and ballast load resistance is infinity (no load). The effective value of ballast resistance can be varied to any value between no load (infinite resistance) to full load, by varying the duty ratio from zero to unity. The variation in the main load results in variation in the line voltage (V_t or V_{yr}). This variation in the line voltage is sensed and the duty ratio D of the switch S is varied on closed loop. In this way, the sum of main load and ballast loads is maintained nearly constant. The output power is also maintained constant. Voltage and frequency are thus regulated. Following assumptions are made to carry out dynamic analysis:

1. The DC side resistance is transferred to the AC side. The switching frequency is very high (25 kHz). The effective ballast resistance is equal to R_a/D.

2. The load-balancing elements (Section 3) are designed for load resistance corresponding to maximum load (full load). In case of small-signal model, it is assumed that the generator always operates at full load (perturbations are small). Therefore, voltages and currents in the generator are always balanced.

3. The turbine dynamics is slow compared to the dynamics of the electric circuit (i.e. mechanical time constant is larger than electrical time constant). When the main load is disturbed, the line voltage and speed of the turbine vary. The variation in line voltage will take
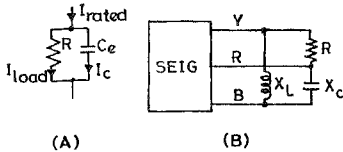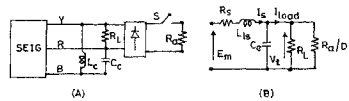
Fig 3.   Fig 4.

place faster on account of the smaller electrical time constant. The change in speed of the turbine will be slower because of larger mechanical time constant. To maintain a constant line voltage a fast controller is implemented (controller time constant is comparable with electrical time constant). Variations in the speed of the turbine are neglected.

4. For small-signal model, disturbance in magnetizing emf (E_m) can be neglected. The approximate per-phase equivalent circuit (after all these assumptions) is shown in Fig. 4.

The dynamic behaviour of the circuit (Fig. 4) is determined. It is a second-order system. The PI-controller is designed based on transfer function approach. The system is non-linear and this approach is applicable only for small-signal model of the system. An elaborate dynamic model has been described in Section 2. The verification of this simplified dynamic analysis of the system is done through detailed simulation (using dynamic model of Section 2).

5. Simulation results

a) *Steady-state response*: Following observations from no-load to full-load transition.

   1. All line voltages in SEIG (steady state) are regulated within 2%, machine currents are regulated within 4% and there is no appreciable change in frequency.

   2. Unbalance (steady state) in machine currents and line voltages (across machine terminals) is less than 4 and 1%, respectively.

b) *Transient response*: The step response (transition from full load to 60% of full load) shows that there is a small overshoot of around 3% in voltage and the settling time (T_s) is one and a half cycles (30 ms).

6. Test results

a) *Steady-state response*: Following observations from no-load to full-load transition.

   1. All line voltages (steady state) are regulated within, machine currents are regulated ±3% and there is no appreciable change in frequency.

   2. Unbalance (steady state) in machine currents and line voltage (across the machine terminals) is less than ±8 and ±4%, respectively.

b) *Dynamic response*: The step response for transition from full load to 50% of full load is as follows:

There is an overshoot of around 24% and the settling time (T_s) is 5 to 6 cycles (120 ms).

7. Conclusions

Finally, on the basis of experimental and simulation results it can be concluded that a self-excited induction generator can be used for MHPP. A satisfactory voltage regulation and a good frequency regulation is achieved. The voltage feedback control strategy is effective. A 2.2 kW machine could be loaded up to 1.8 kW. The maximum unbalance in the line voltages was ±4% and line currents was ±8%. The generator is operated at a lower power output as compared to the actual rating of induction machine (15–20% derating for the given case). However, the cost of induction machine is much less compared to alternators. Therefore, the whole set-up may turn out to be a cost-effective option.

References

1. ELDER, J. M., BOYS, J T. AND WOODWARD, J. L   Process of self excitation in induction generator, *IEE Proc. B*, 1983, **130**(2), 103–108.

2. SAY, M. G.   *The performance and design of alternating current machine*, CBS Publishers and Distributors, 1983 (Indian edition)

3. ELDER, J. M, BOYS, J T. AND WOODWARD, J. L   Self excited induction machine as a low cost generator, *IEE Proc. C*, 1984, **131**(2), 33–41

4. GRANTHAN, C , SUTANTO, D. AND MISMAIL, B   Steady state and transient analysis of self excited induction generator, *IEE Proc. B*, 1989, **136**, 61–68.

5. LEONHARD, W   *Control of electric drives*, Springer-Verlag, 1985.

Thesis Abstract (M. Sc. (Engng))

Criteria for advertising agency selection in India: An objective appraisal by Priyadarshini Mudnal

Research supervisor: Profs R. Srinivasan and N. Somasekhara
Department: Management Studies

1. Introduction

Evaluation of advertising agency (ad agency), either for the purpose of selecting or auditing, is an expensive, traumatic and time-consuming exercise for the advertiser. This is so because the advertiser is actually locating, recruiting, evaluating and selecting another company to be its marketing partner. The problem is compounded by the fact that most managers do not have the experience in finding and selecting advertising agencies and could use some tips to make the process more effective. It is helpful to develop some criteria about what the advertiser wants and then match his needs with an agency that has appropriate resources. In short, a marketing partner who will be a good fit for the advertiser has to be identified. Advertisers usually hire the advertising agencies for the following services: market research, marketing or strategic market planning, media planning/scheduling, creative work, account management, TV film/radio production.

2. Need for the study

The need for this study arose not only because of paucity of studies in the area of advertising agency (client) relationship in India but also due to the following reasons:

1. Agency/client relationship is very important but is a neglected area of promotion.

2. It is of prime importance for the advertiser to study the attributes they see as crucial to their relationship with an ad agency to form an overall evaluation of the agency.

3. A long-term partnership is necessary for the advertiser to help grow business through effective advertising and for the agency to participate in strategic marketing.

4. To meet the growing needs among the advertisers and the ad agency for a continuous monitoring system which would provide a feedback on the efficiency and effectiveness of the ad agency services to the advertiser's marketing activities.

3. Objectives

There is a paucity of studies where one can determine quantitatively the factors which influence the selection criteria given a firm's organisation and marketing environment. This work by way of empirical research aims at studying strategic aspects of selection criteria used by Indian advertisers while selecting or evaluating an ad agency.

The objectives addressed in this study are: a) to determine, quantitatively, factors which the advertisers use to assess the capabilities of current and prospective agencies. b) to examine the relationships between the selection of an ad agency and the firm's internal characteristics, specifically, sales revenue, ad expenditure as a percentage of sales and product classification, and (c) to address marketing policy implications as a result of the above two aspects.

4. Methodology

The study draws on the work of Cagley and Roberts[1] selection criteria for US firms. The study is empirical in nature with an ex-post-facto design. A random sample of 380 firms was drawn and a questionnaire was mailed to advertising and marketing managers. Seventy-seven completed questionnaires were returned and served as database for the study. The sample consisted of consumer (non-durable and durable goods) and industrial firms.

The plan of analysis focussed on a) an analysis of relative importance of agency attributes, and b) preliminary examination of the interrelationships among the attributes.[2]

Three hypotheses were formulated based on discussions with advertising agencies, marketing managers and survey of existing literature. These related to differences in perceived importance of the ad agency attributes of firms which were classified according to annual sales, ad expenditure as a percentage of sales and self-classified firms as consumer or industrial. Firms with Rs. 3 billion and over per year formed one category and those less than Rs. 3 billion per year another. The firms were also split using advertising rupee as a percentage of sales. The ratios were split at 2% of sales.

5. Results and inferences

Descriptive analysis and testing of hypothesis yield the following inferences:

- The study strongly affirms the importance of people factor as a criterion measure in the evaluation/selection process employed by a majority of firms. Key elements that emerge from the data are personnel quality, reputation, integrity, mutual understanding and agreement, interpersonal compatibility and synergism.

- Larger firms when classified by size of sales revenue placed greater importance on market planning, agency stability, marketing philosophy, full range of services. Larger firms prefer association with agencies similar in size and capabilities to themselves.

- Firms which have a higher share of advertising expenditure prefer a greater partnership in terms of interaction and top management participation. The product classification too has a practical effect upon perceptions reported.

- A factor analysis of the data was performed to discover how the 25 variables correlate thereby determining the underlying dimensions of ad agency–client relationship. Eight general factors were derived by principal component analysis with iteration and varimax rotation.

6. Conclusions

It can be generally concluded that a) people factor is the most important criterion measure in the evaluation/selection process employed by a majority of firms, and b) firm's internal characteristics, i.e. sales, ad expenditure as a percentage of sales and product classification influence the selection criteria of the advertisers.

References

1. CAGLEY, J. AND ROBERTS, R.   Criteria for ad agency selection: An objective appraisal, *J. Advtg*
   SHAPIRO, A. H.   *Res.*, April/May 1984, **24**(2), 27–31.

2. HOTZ, M , RYANS, J. AND   Agency/client relationships as seen by influentials on both sides,
   SHANKLIN, W.   *J. Advtg*, 1982, **1**(2), 37–44.

Thesis Abstract (M. Sc. (Engng))

Wavelength routing in all-optical networks using full, limited and no wavelength conversion by Tushar Tripathi
Research supervisor: Prof. Kumar N. Sivarajan
Department: Electrical Communication Engineering

1. Introduction

Wavelength-routing networks that employ wavelength division multiplexing have emerged as the most attractive type of all-optical networks. Wavelength-routing networks offer the advantages of wavelength re-use and scalability over broadcast-and-select networks and are therefore suitable for wide area networks (WANs). A wavelength-routed network that allows any user to be connected to any other user without intermediate optical-to/from-electrical conversion is referred to as an all-optical wavelength routed network. It is clear that users will eventually

need networks that connect hundreds or thousands of nodes, each running at gigabit speeds. The all-optical approach immediately opens up the possibility of systems with thousands of users per link or network, each running at gigabit speeds, and yet employing electronic and photonic components whose speed need not be greater than the per-node bit rate.

There has been considerable interest in obtaining the call-blocking performance of wavelength-routing networks. The quantification of the performance improvement obtainable with wavelength converters is of fundamental importance. A number of papers addressing this issue have appeared in the literature.[1-3] A traffic model that considers the effects of path length, switch size, and interference length on the wavelength utilization in the presence and absence of conversion was presented by Barry and Humblet.[3] A model to iteratively evaluate the blocking probabilities for dense networks with and without wavelength conversion was presented by Birman.[2]

The main problem in optical networks is that the wavelength conversion at the optical node is difficult. Then the same wavelength should be assigned to the connection on all the links along the route if a capability of wavelength conversion is not provided at the switching node. This requirement is referred to as the *wavelength continuity constraint*. Birman compared the performances of a fixed routing method with and without wavelength conversion, and it is shown through approximate analysis and simulations that the fixed routing method without wavelength conversions remarkably degrades performance in terms of call-blocking probability. Ramaswami and Sivarajan[1] derived a lower bound for blocking probabilities for any routing and wavelength-assignment algorithm with and without wavelength translation. In all these studies, it has been stated that the performance improvement gained by employing wavelength conversion can be large, but is strongly dependant on many factors.

These models considered networks that have full wavelength conversion capability at every node or networks without any conversion capability. Because of the increased complexity and cost of a routing node with wavelength conversion, a limited amount of wavelength conversion may be attractive in practice. Limited wavelength conversion can imply a limit on the number of wavelength conversions allowed per node, or on the number of nodes with full wavelength conversion capability (sparse wavelength conversion), or on the range of wavelengths to which a given wavelength can be converted.

2. Problem statement and formulation

We have tried to investigate this issue further. The research problem is concerned with routing in all-optical networks using full, limited and no wavelength conversion. The problem addresses whether it is possible to achieve comparable performances using no or limited conversion to full conversion. It also addresses one more important issue whether it is always beneficial to use full wavelength conversion as opposed to no or limited wavelength conversion. The index of performance measure considered is blocking probability of the arrivals. We consider networks operating in circuit-switched mode. The model chosen for performance analysis is lossy one in the sense that if calls are blocked then they are dropped and cleared. Each call is accepted only if all the links on its route have enough resources to support the call. The arrivals are taken to be Poisson and holding time is exponentially distributed with unit mean.

We formulate an exact model for small linear tree networks (especially two- and three-link tandem networks) based on Markov chain theory for both the full and no-wavelength conversion cases. We derive an exact analytical expression for the computation of blocking probability. The results obtained show that the blocking probability Pb, while using full conversion is less than that of the no conversion case up to a certain point after which it is surprisingly the other way around. Moreover, this point which we call *crossover point* decreases as the number of wavelengths is increased. The crossover point goes down because of *trunking efficiency*, i.e. increasing the number of wavelengths per link in the network will obviously lead to decrease of blocking probability for both the cases, full and no conversion; therefore, the crossover point also decreases.

The reason that this crossover occurs (consider the two-link tandem network) is due to the fact that initially we may have fewer calls using both the links in the case of no conversion because of wavelength continuity constraint evens though we may have free wavelengths on both the links (but not the *same* wavelength free on both the links). Consequently, higher blocking results in the no conversion case, whereas, for the same situation, we can carry the same call (calls using both the links) in the case of full conversion since it needs only *a* free wavelength on both the links.

The crossover can't happen in principle if we use optimal algorithms since we can always pretend that we don't have the converters but the point is that many analyses of the effect of wavelength conversion assume certain suboptimal routing algorithms and take for granted that wavelength conversion can only help. The results obtained show that it can sometimes hurt under the *same* routing algorithms.

The exact model considered cannot be used to analyze bigger networks because of the large dimensionality. As the size of the network increases it becomes almost impossible to analyze as the size of state space quickly blows up. Due to this fact, we use the approximate model of Chung *et al.*[5] to analyze the full conversion case and an approximate model developed by Birman[2] to analyze no conversion case. Both these models are based on a *generalized state-dependent reduced load approximation*. In these schemes, it is assumed that blocking occurs independently from link to link and that the offered traffic to a given link is Poisson but thinned by blocking on other links. This leads to a set of nonlinear fixed-point equation with approximate blocking probabilities at various links as unknown variables. Repeated substitution is employed to solve fixed-point equations. Using these models, we analyze some bigger networks and find that the results obtained are similar to what we already stated above while using the exact model. These results were also verified by corresponding simulations.

We find that this crossover does not occur below 10% blocking level. However, most of the time we are only interested in having at most 2 or 3% blocking probability. At these low blocking levels full wavelength conversion outperforms the no wavelength conversion. Although full wavelength conversion is desirable as it decreases blocking probability, it is difficult to implement in practice due to technological limitations. Since all-optical converters are still being prototyped in laboratories and are likely to remain expensive, researchers have turned their attention to searching for suitable alternatives. A recent analysis by Subramaniam *et al.*[6] found that there is no significant degradation in the network performance even when only a

few nodes of the network have the full conversion capability. Yates *et al.*[4] were the first to present a simple, approximate probabilistic analysis to study the effect of limited-range conversion on the blocking probability of a single path consisting of two or more hops and used simulations to examine the effects of limited-range conversion on the blocking probability of networks for fixed routing.

All-optical wavelength converters with limited conversion range permit an incoming wavelength to be switched only to a small subset of the outgoing wavelengths. Using a graph-theoretical approach, we derive an analytical model for limited wavelength conversion by extending the idea presented by Birman[2] for fixed routing. Using this model, we assess analytically the network performance improvements using limited wavelength conversion. This analysis can be applied to any network topology.

We assume that for any given input wavelength, it is possible to translate it to a limited range of output wavelengths. More precisely, it is assumed that a wavelength can be converted to d adjacent wavelengths on either side of the input wavelength, including the wavelength itself, where d is the degree of conversion. Hence, any wavelength can be converted to $2d + 1$ wavelengths. For example, incoming wavelength λ_l can be converted to any of the outgoing wavelengths $\lambda_{(l-d)}, \ldots, \lambda_l, \ldots, \lambda_{(l+d)}$.

We consider a network with an arbitrary topology with J links and C wavelengths on each link. A route R is a subset of links $1, \ldots, J$. Calls arrive for route R as a Poisson stream with rate a_g. An incoming call on route R is set up if it finds a free wavelength on all the links from the possible choices of outgoing wavelengths with the given degree of limited wavelength conversion. If such a combination of wavelengths is not possible on all the links constituting the path, then the call is blocked and lost. If the call is accepted it simultaneously holds the wavelength(s) on all the links on route R for the duration of the call. The holding times of all the calls is assumed to be exponentially distributed with unit mean. We have considered only simplex connections even though the model may be adaptable for duplex connections also.

We analyze the case where an incoming wavelength can be switched to one of $d = 1$ or 2 outgoing adjacent wavelength on either side of the incoming wavelength. We find that d-adjacent wavelength switching with only $d = 1$ or 2 suffices to give performance significantly superior to that obtained with no wavelength conversion and very close to that of full wavelength conversion. The results that we obtain are very close to the corresponding simulation results, and predict network performance over a wide range of network loads. By contrast, Yates *et al.*[4] had predicted, based on their simulation, that limited wavelength conversion of degree $\pm 50\%$ would be needed to give performance nearly equal to that of full wavelength conversion.

3. Results and discussion

We present simulation and analytical results for a 6-node ring network, and an example network with 6 nodes and 7 links for three different cases: no wavelength conversion, limited wavelength conversion with degree $d = 1$, 2, and full wavelength conversion. In all cases, limited conversion provides a considerable fraction of the improvement that the full wavelength conversion case provides over no wavelength conversion.

For the 6-node example network, we plot the graphs for 8 and 16 wavelengths to study the effect of full, no and limited wavelength conversion. We see that limited wavelength conversion with degree $d = 1$ (for 8 wavelengths) provides almost the same performance as that of full conversion. It is also shown that limited conversion provides an improvement that is much better than that of no wavelength conversion. We further show that our analysis results for limited conversion matches with the results obtained by simulation. For the 16 wavelength case, with conversion degree $d = 2$, we show that the difference in performance between full and limited wavelength conversion is almost zero. In subsequent figures, we show that our analysis and simulation result match quite well. To give a more clear picture of accuracy we plot the difference curve of analysis and simulation results. The difference is of the order of 10^{-3}.

For the 6-node ring network, with conversion degree $d = 1$, we show that we can achieve the same performance as that of full conversion. It is also shown further that the analysis and simulation results match quite well. Again, by plotting the difference curve for analysis and simulation we show that the difference is of the order of 10^{-3}.

4. Conclusions

Though we have presented two examples to show the benefits of limited wavelength conversion, we feel that for almost all kinds of network topologies, limited conversion provides a marked improvement in the locking performance of the network as compared to no wavelength conversion. Furthermore, the performance obtained by limited conversion with either $d = 1$ or $d = 2$ is very close to the blocking performance of the network with full wavelength conversion.

The computational requirements of the wavelength routing model and limited wavelength conversion presented are significant. The technique of *truncated distribution* could be applied here as well, and will alleviate the problem somewhat for moderate and heavy traffic. Other ways to reduce the computational requirements are by using a parallel implementation of the method presented (or any other fixed-point algorithm). The analytical model derived for limited wavelength conversion can also be used for alternate routing with limited wavelength conversion.

In conclusion, our new analytical model for limited wavelength conversion is much more accurate than the models developed hitherto for the case of no wavelength conversion. Comparison with simulations in two example networks show that the difference between the performance predicted by our approximate analytical model and simulations is in the range 0.001–0.003 for the blocking probability in the range.

References

1. RAMASWAMI, R. AND SIVARAJAN, K. N   Routing and wavelength assignment in all-optical networks, *IEEE/ACM Trans. Networking*, 1995, **3**, 489–500.

2. BIRMAN, A.   Computing approximate blocking probabilities for a class of all-optical networks, *IEEE J.*, 1996, **SAC-14**, 852–857.

3. BARRY, R. A. AND HUMBLET, P. A.   Model of blocking probability in all-optical networks with and without wavelength changers, *Proc. IEEE INFOCOM'95*, pp. 402–412.

4. YATES, J. *et al.*   Limited-range wavelength translation in all-optical networks, *Proc IEEE INFOCOM'96*, pp. 954–961.

5 CHUNG, S. P. *et al.*   Computing approximate blocking probabilities for large loss net works with state-dependent routing, *IEEE/ACM Trans. Networking*, 1993, 105–115.

6. SUBRAMANIAM, S., AZIZOGLU, M. AND   All-optical networks with sparse wavelength conversion, *IEEE/ SOMANI, A. K.*   *ACM Trans. Networking*, 1996, 544–557.

Thesis Abstract (Ph.D.)

Molecular dynamics simulations of O-linked oligosaccharides from respiratory-mucus glycoproteins by M. Jagannatha Rao
Research supervisors: Profs Saraswathi Vishveshwara, V. S. R. Rao and P. Venkataram
Department: Molecular Biophysics Unit

1. Introduction

Mucus glycoproteins, also known as *mucins*, contain oligosaccharide chains in which the sugar residue N-acetyle-galactosamine (GalNAc) is covalently attached to the side-chain hydroxyl oxygen atom in serine or threonine on the polypeptide chain (O-Linked oligosaccharides). These O-glycans are polydisperse, linear and flexible threads (80 to 3000 nm) and show extreme microheterogeneity and inhibit binding and helix formation of the polypeptide chain. The rod-like shape of mucins is believed to contribute to major physicochemical property of mucins, namely, viscoelasticity which manifests in the protective and lubricative properties of mucins. O-glycans bind to the pathogenic bacteria, parasites and toxins and at times mimic the natural binding sites of pathogens, thus preventing the pathogens from binding to the mucosa.[1]

Mucin oligosaccharides occur in neutral and acidic forms. Commonly found non-fucosyl sugar residues in mucins are GalNAc, N-acetyl-glucosamine (GlcNAc), galactose (Gal) and fucose (Fuc). Gal and GlcNAc may be sulphated or phosphated and compete with sialic acid (Sia) to the acidity of some mucin-type oligosaccharides. Fuc and Sia appear in α-linkage while the non-fucosyl residues appear in β-linkage. Using samples isolated from pathological specimens, O-glycans have been classified into six categories (Core type 1, type 2,..., type 6) based on the central core structure (Fig. 1). The mucin core structures appear to be tissue/species specific. For example, O-glycans with Core types 3 and 4 structures have been found in humans and only Core type 4 in patients suffering from chronic bronchitis. Oligosaccharides possessing more than eight residues have been described in human colonic,[2] gastric[3] and ovarian cyst mucins.[4] Also, these O-glycans contain, at the nonreducing end, Lewis blood-group determinants (Le^a, Le^b, Le^x, Le^y). Highly specific glycosyl-transferases are responsible for the synthesis of a number of core structures. Partial structures of O-glycans have been studied by theoretical methods such as potential energy calculations and experimental techniques (NMR) to understand their conformational preferences. While it is difficult to explore the complete energy surface of oligosaccharides using potential energy computations, only average conformational features can be obtained using NMR. Also, the inherent difficulties in crystallizing oligosaccharides forms a bottleneck in the understanding of the 3D shapes of these molecules, which is very essential to study the interactions of oligosaccharides with other bio-

polymers. In order to address the above issues, molecular dynamics (MD) simulations of O-linked oligosaccharides (7–9 residues in length) from the respiratory-mucus glycoproteins extracted from the sputum of a patient suffering from bronchiactasis due to Kartegener's syndrome[5] have been undertaken.

2. Materials and methods

The structures of the O-linked oligosaccharides have been generated in the computer using in-house software. All D-sugar residues have been considered in $^4C_1$ chair and the Fuc residue in $^1C_4$ chair conformation. An initial value of 117.5° was set for the interunit glycosidic bond angle. All N-acetamido groups in the GalNAc and GlcNAc residues were fixed using the standard Pauling–Corey geometry[6] with the amide bond in a *trans* conformation. For the $(1 \rightarrow 6)$ linkage, three starting conformations were considered with values for the torsion angle χ equal to 60°, –60° and 180°. InsightII/Discover suite of programs (Biosym® Technologies) was used for potential energy minimization and MD simulations. All the generated structures were minimized, using the method of steepest descents (200 steps) to relieve any possible strain in the molecule. This was followed by the potential energy minimization and MD simulations.

Galβ(1-->3)GalNAcα   Core Type 1

GlcNAcβ(1-->6)
                \
                    GalNAcα   Core Type 2
                /
   Galβ(1-->3)

GlcNAcβ(1-->3)GalNAcα   Core Type 3

GlcNAcβ(1-->6)
                \
                    GalNAcα   Core Type 4
                /
GlcNAcβ(1-->3)

GalNAcβ(1-->3)GalNAcα   Core Type 5

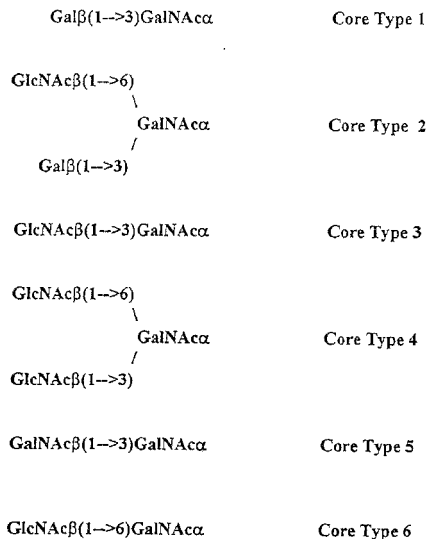GlcNAcβ(1-->6)GalNAcα   Core Type 6

FIG. 1. Schematic diagram showing the classification of O-linked oligosaccharides based on their core structure.

All the generated structures were minimized, using the method of steepest descents (200 steps) to relieve any possible strain in the molecule. This was followed by the potential energy minimization using the conjugate gradients technique till a maximum derivative equal to 0.001 kcal/Å was reached. The default CVFF force field was used for all computations. The total potential energy of the molecule was calculated as a sum of contributions from bond stretching, bond angle bending, torsional strain, van der Waals and electrostatic components. Interactions among all the nonbonded atom pairs were calculated without using any distance cutoff criteria. A distance-dependant dielectric constant (= 4*r) was used (as it weighs the short-range interactions more than the long-range interactions) while computing the electrostatic interactions. All the minimized structures were then subjected to constant energy MD simulations (40 ps equilibration followed by 500 ps productive run) in vaccum at 300 K without explicit water. A time step of one femtosecond (fs) was used for integration which was performed using the Verlet's Leap-frog algorithm[7] and coordinates history was collected at 300 fs intervals.

3. Results and discussion

The seven O-linked oligosaccharides studied have been, for purposes of discussion, grouped as Set-I (designated as D, S1, S2 and S3) (Fig. 2a) and Set-II (designated as S4, S5 and S6) (Fig. 2b). The glycosidic torsion angle vs time trajectories for all linkages was generated. A number of snapshots were collected from the MD data. The conformational angles (ϕ, ψ) at the various linkages were computed and plotted in the corresponding conformational maps. Analysis of the trajectories and the (ϕ, ψ) maps reveals that the torsion angle χ in the (1 → 6) linkage generally prefers values around –60°. Also, the torsion angle ψ is more flexible and has a larger degree of freedom of rotation compared to ϕ or χ in the (1 → 6) linkage. The β(1 → 3/4)-linked disaccharide segments access conformations from regions in the allowed (ϕ, ψ) space, which are, however, slightly shifted from the disaccharide MD average value. Such observed shifts could perhaps be attributed to the location of the linkage in the oligosaccharide and/or the environment around the linkage. The conformationally allowed region for the disaccharide GlcNAcβ(1 → 3)GalNAc is much smaller than the other β(1 → 3/4) or α(1 → 2/3/4)-linked disaccharide segments. This reduction in the allowed conformational space is due to the presence of the two N-acetamido groups in the above disaccharide segment.

An analysis of the snapshots of the Set-I oligosaccharide structures has revealed the existence of a range of conformations accessed during the simulations. These range from a fully stretched (extended) to a very compact shape. The terminal residues are often involved in hydrogen bond interactions with distal residues whenever a compact shape is assumed by the oligosaccharides. Also, when these fragments fold (or loop) back to form a compact shape, stacking interactions are observed. In a majority of the MD simulations, the Le^b-tetrasaccharide segment in Set-I oligosaccharides has been found to assume conformations similar to those observed in the isolated Le^b simulations with 'face-to-face' interactions between the residues Gal and Fuc attached to GlcNAc. However, in some cases, 'edge-to-face' stacking interactions have also been observed.

Analysis of the MD simulation data corresponding to Set-II oligosaccharides has shown that, as in the previous case, the various disaccharide segments comprising these oligosaccha-
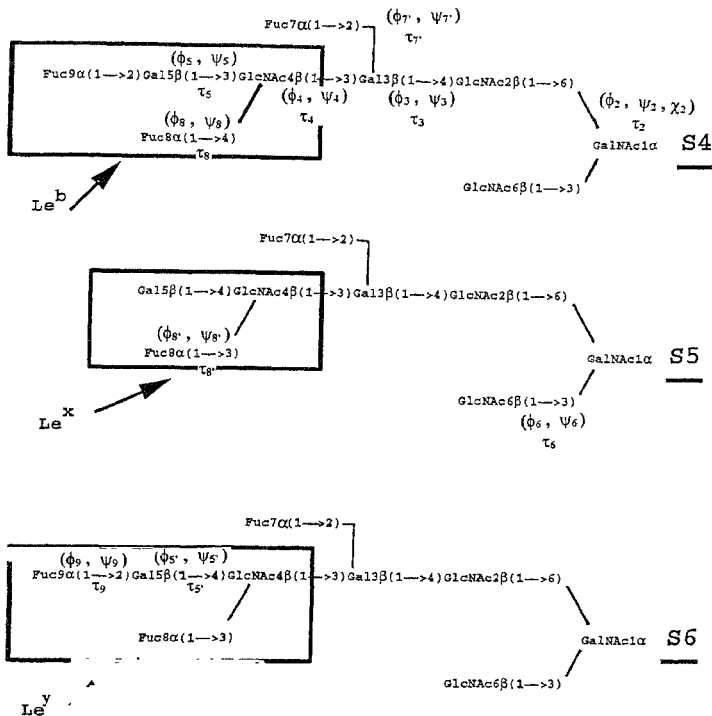
FIG. 2a. Schematic diagram showing the structures of O-linked oligosaccharides from the respiratory-mucus glycoproteins.

Structures designated D, SI, S2 and S3 are referred to as Set-I oligosaccharides in the text. Numbering of the sugar residues is arbitrary. The principal torsion angles (ϕ, ψ, χ) are marked along side of the disaccharide fragment and τ is the glycosidic bond angle (residue number of the anomeric carbon atom is used as a subscript to the torsion angle symbols).

rides also access conformations well within the generally allowed regions from the respective (ϕ, ψ) map, but also from neighboring sub regions in the conformationally allowed space. Such a trend suggests that the general notion that substitutions on adjacent carbon atoms in monosaccharide units reduces the conformational flexibility due to steric hindrances need not necessarily be valid at all times. Environments such as the one around the Gal3 residue in Set-

FIG. 2b. Schematic diagram showing the structures of O-linked oligosaccharides from the respiratory–mucus glycoproteins

Structures designated S4, S5 and S6 are referred to as Set-II oligosaccharides in the text. Numbering of the sugar residues is arbitrary. The principal torsion angles (ϕ, ψ, χ) are marked along side of the disaccharide fragment and τ is the glycosidic bond angle (residue number of the anomeric carbon atom is used as a subscript to the torsion angle symbols).

II oligosaccharides might shift the accessible conformations to a nearby region in the (ϕ, ψ) map and make available more conformations by reducing energy barriers between the various local minima and global minimum. The disaccharide segment Fuc$\alpha(1 \rightarrow 4)$GlcNAc in Set-II oligosaccharides has been found to assume two distinct conformations with values for (ϕ, ψ) around (45°, 25°) and (−25°, −30°). Similarly, the Fuc$\alpha(1 \rightarrow 3)$GlcNAc segment has been found to assume conformations around (50°, 25°) that are altogether different from those as-

sumed by this segment during the isolated Le^x/Le^y simulations with (α, ψ) around ($-30°$, $-25°$). These different conformations assumed by fucosyl segments when they are part of larger structures manifest in the different conformations assumed by these blood-group determinants.

An analysis of the snapshots of the Set-II oligosaccharide structures obtained from the MD simulation data has revealed the possibility of conformations with various shapes for these oligosaccharides. Most of the time, the Set-II oligosaccharides assume linear (i.e. stretched) conformations with compact shapes being observed only occasionally, which is in contrast to the conformations of Set-I oligosaccharides wherein compact shapes are predominant and extended shapes are less frequent. The above preference in the conformations observed by Set-II oligosaccharides appears to be due to the presence of the Fucosyl residue in the proximity of the $\beta(1 \to 6)$ linkage in these molecules.

Reference

1 ROUSSEL, P. *et al.*   *Biochimie*, 1988, **70**, 1471.

2 PODOLSKY, D. J   *J. Biol. Chem.*, 1985, **260**, 8262

3 SLOMIANY. B L , ZDEBSKA, E AND   *J Biol. Chem.*, 1984, **259**, 2863.
   SLOMIANY, A.

4. KLEIN, A. *et al.*   *Eur. J Biochem* , 1988, **171**, 631.

5 KLEIN, A. *et al.*   *Eur. J. Biochem* , 1991, **198**, 151

6 COREY, R B. AND PAULING, L   *Proc. R. Soc. Lond B*, 1953, **141**, 10.

7 VERLET, L.   *Phys Rev.*, 1967, **159**, 98.

Thesis Abstract (Ph. D.)

Crystal structure, carbohydrate specificity and quaternary association of basic agglutinin from winged beans by Moses Mohandas Prabu
Research supervisors: Dr. K. Suguna and Prof. M. Vijayan
Department· Molecular Biophysics Unit

1. Introduction

Lectins are multivalent carbohydrate-binding proteins of non-immune origin.[1] In recent years, there has been a spurt in lectin research on account of their ability to specifically bind to cell surface carbohydrates and in view of their diverse applications. The richest sources of lectins are the seeds of leguminous plants, but they are found in all classes and families of organisms. Legume lectins share the same tertiary structure. Out of the four loops that come together to form the sugar-binding site, three are conserved in all the legume lectins of known structure while the fourth, which is variable, is believed to confer specificity. In addition to their diverse carbohydrate specificities, these lectins also exhibit a variety of modes of quaternary association, which is of particular interest. In this context, the current study seeks to elucidate the factors responsible for the variability in subunit association of legume lectins and the role of the

variable loop in generating sugar specificity, using basic agglutinin from the seeds of winged beans (*Psophocarpus tetragonolobus*) (WBAI) as a model.

2. Experimental

WBAI is a homodimer with molecular weight of 58,000 Da and 241 amino acid residues. The protein is glycosylated at two positions and has a pI > 9.0. The lectin agglutinates human type **A** and **B** but not type **O** erythrocytes. Earlier work in this laboratory on WBAI resulted in three crystal forms,[2] of which an orthorhombic form (space group $P2_1=2_12$; $a = 155.5$, $b = 92.3$ and $c = 72.5$ Å) complexed with methyl-α-D-galactopyranoside was used for intensity data collection and structural studies. Diffraction data were collected on a Siemens–Nicolet area detector system mounted on a GX-20 Marconi Avionics rotating anode X-ray generator. The raw data were processed using the XENGEN package. The data extended to 2.5 Å R_{merge} 6.4% and had a completion of 77.3%.

The structure of WBAI with two dimeric molecules in the asymmetric unit was determined using molecular replacement using MERLOT package with *Erythrina coralladendron* lectin (*EcorL*)[3] as the model. The structure was refined using the program X-PLOR and the model was fitted into the electron density using FRODO. The refined model consists of 8143 non-hydrogen atoms which also includes 546 water oxygens. The R-factor of the refined structure is 18.7% for 28,257 reflections, with root mean square deviations of 0.010 Å, 1.8° and 27.3° from ideal values in bound lengths, bond angles and dihedral angles, respectively.

3. Results and discussion

Each subunit of WBAI consists of the characteristic legume lectin tertiary fold.[4] Careful examination of the sugar-binding site revealed that the length and the conformation of the long variable loop observed in WBAI will pose steric hindrance to sugars with β-substituents at the anomeric position. Simple modelling of the blood group determinants of **A**, **B** and **O** at the sugar-binding site, in addition to a comparison with *EcorL* and peanut agglutinin (PNA),[4, 5] another lectin in the family, clearly demonstrates the role played by the variable loop in dictating lectin's specificity for the α-galactose at their terminus bind to WBAI while **O** is not recognised as the linkage is β.

The major interest in the mode of dimerisation of WBAI is in relation to determining the relative importance of glycosylation and features intrinsic to the protein, in the variability exhibited by legume lectins in quaternary association. The glycosylation site in *EcorL* is at the interface between the two monomers in the canonical dimer, which is believed to be the favoured mode of association in legume lectins. Therefore, this mode of dimerisation cannot occur in *EcorL*. The glycosylation sites in WBAI are far away from this interface and cannot possibly affect the formation of canonical dimers. However, if the mode of dimerisation is determined by the features of the protein itself, WBAI is likely to form an *EcorL*-type dimer in view of the high-sequence homology between the two lectins. The crystal structure demonstrates that this is indeed the case. The WBAI structure,[6] and the earlier work on PNA,[4, 5] conclusively demonstrate that legume lectins are an interesting family of proteins in which small alterations in essentially the same tertiary fold lead to large changes in quaternary structure.

Relationships among the modes of subunit association in different legume lectins have also been analysed. The role of factors such as buried accessible surface area, interaction energies and shape complementarity in determining the mode of oligomerisation has been elucidated.

4. Appendices

In parallel, the author also has participated in an ongoing small-molecule project which involves the preparation and X-ray structure determination of the complexes of carboxylic acids with L- and DL-forms of amino acids. As part of this project, the complexes of DL- and L-histidine with oxalic acid were analysed and a comparative study of amino acid–oxalic acid complexes was carried out.[7-9] An Appendix deals with the alignment of legume lectin sequences on the basis of three-dimensional structures.

References

1. SHARON, N. AND LIS. H.   *Science*, 1989, **246**, 227–246.

2. SANKARANARAYANAN, R *et al.*   *J. Mol. Biol.*, 1993, **229**, 558–560.

3. SHAANAN, B., LIS, H. AND SHARON, N.   *Science*, 1991, **254**, 862–866.

4. BANERJEE, R. *et al*   *Proc. Natn. Acad. Sci. USA*, 1994, **91**, 227–231.

5. BANERJEE, R. *et al.*   *J Mol. Biol.*, 1996, **259**, 281–296.

6. PRABU, M. M. *et al.*   *J. Mol Biol.*, 1998, **276**, 787–796.

7. PRABU, M. M., NAGENDRA, H. G.,   *J. Biomol. Struct Dyn* , 1996, **14**, 387–392.
   SURESH, S. AND VIJAYAN, M.

8. VENKATARAMAN, J., PRABU, M M   *J. Pept. Res.*, 1997, **50**, 77–87
   AND VIJAYAN, M.

9. CHANDRA, N. R. *et al.*   *Acta Cryst B*, 1998, **54**, 257–263.